

Correlating geometry, microstructure and properties of High Strength Steel thin wall structures fabricated with WAAM

Babu, Aravind; Trodini, Emiliano; Argumedo, José Luis Galán; Richardson, Ian M.; Hermans, Marcel J.M.

DOI

[10.1016/j.jajp.2025.100292](https://doi.org/10.1016/j.jajp.2025.100292)

Publication date

2025

Document Version

Final published version

Published in

Journal of Advanced Joining Processes

Citation (APA)

Babu, A., Trodini, E., Argumedo, J. L. G., Richardson, I. M., & Hermans, M. J. M. (2025). Correlating geometry, microstructure and properties of High Strength Steel thin wall structures fabricated with WAAM. *Journal of Advanced Joining Processes*, 11, Article 100292. <https://doi.org/10.1016/j.jajp.2025.100292>

Important note

To cite this publication, please use the final published version (if applicable). Please check the document version above.

Copyright


Other than for strictly personal use, it is not permitted to download, forward or distribute the text or part of it, without the consent of the author(s) and/or copyright holder(s), unless the work is under an open content license such as Creative Commons.

Takedown policy

Please contact us and provide details if you believe this document breaches copyrights. We will remove access to the work immediately and investigate your claim.



Correlating geometry, microstructure and properties of High Strength Steel thin wall structures fabricated with WAAM

Aravind Babu ^{*}, Emiliano Trodini, José Luis Galán Argumedo, Ian M. Richardson, Marcel J.M. Hermans

Mechanical, Maritime and Materials Engineering, Delft University of Technology, Mekelweg 2, 2628 CD, Delft, The Netherlands

ARTICLE INFO

Keywords:

Wire arc additive manufacturing
Heat input
Geometry
Microstructure
Cooling rate
Mechanical properties

ABSTRACT

Wire arc additive manufacturing (WAAM) of high-strength steel (HSS) has gained significant attention for structural applications. Achieving precise control over the manufacturing process and understanding the relationship between process parameters and the resulting material characteristics is crucial for optimizing the performance of these steel walls to achieve tailored properties. The present study was performed to comprehend the influence of process parameters on the microstructure and properties of wire arc additively manufactured (WAAM) high-strength steel (HSS) thin-wall structures. Multi-layer thin walls of ER110S-G high-strength steel comprising 30 layers were deposited bidirectionally and were fabricated with different travel speeds and wire-feed rates. Geometrical analysis conducted on samples indicates that achieving minimal surface waviness for single-bead thin walls depends on adjusting wire feed rates and travel speeds. Specifically, lower wire feed rates are found to be more effective in minimizing waviness when dealing with single-bead thin walls (thickness < 5 mm). Conversely, lower travel speeds are preferred for reducing surface irregularities in walls fabricated at high deposition rates for thicker single-bead walls (thickness > 8 mm). Cooling rate analysis from midpoints of the 5th, 15th and 25th layers of each sample indicates high cooling rates for low heat input (HI=178 J/mm) samples even for the 25th layer. Microstructural characterization of the samples suggests an increase in acicular ferrite and martensite volume fraction with lower heat input. Additionally, microstructural quantification with EBSD reveals smaller grain sizes and higher Kernel average misorientation for low heat input deposits. Mechanical properties like hardness and tensile strength display an increasing trend with decreasing heat input while elongation to fracture is reduced under the same conditions. Furthermore, anisotropic behaviour is observed in tensile strength and elongation to fracture between building and deposition directions due to the presence of microstructural inhomogeneities.

Introduction

The recent focus on wire arc additive manufacturing (WAAM) arises due to its ability to manufacture large-scale structures with deposition rates as high as 8 kg/h (Wu et al., 2018). Wire arc additive manufacturing involves the integration of an arc welding process, involving a consumable in the form of a wire, with a motion system to deposit molten material along a programmed path. Medium to low complexity designs can be easily manufactured using WAAM, which is associated with low costs for investment and production while a wide variety of wire feedstock material is available. However, in arc welding-based deposition problems might arise due to process instabilities, overheating of samples, and the introduction of residual stresses and distortion, which directly contributes to lower geometrical accuracy compared to

other processes like Laser Directed Energy Deposition (L-DED) (Gisario et al., 2019).

Wire arc additive manufacturing has different variants like GMAW (Gas Metal Arc Welding), GTAW (Gas Tungsten Arc Welding) and PAW (Plasma Arc welding) (Sampaio et al., 2023). GMAW refers to the WAAM process with an electric arc and consumable wire feedstock as electrodes enabling the deposition of large-scale structures. Conversely, GTAW uses a non-consumable tungsten electrode giving higher precision than GMAW. However, GTAW suffers from lower deposition rates and practical difficulties associated with tool-path planning due to the use of an external wire feeder. In the case of PAW, a specialized constricted arc is utilized to obtain a high energy density. This enables better surface finish and lower thermal distortion in components.

^{*} Corresponding author.

E-mail addresses: a.babu@tudelft.nl (A. Babu), m.j.m.hermans@tudelft.nl (M.J.M. Hermans).

<https://doi.org/10.1016/j.jajp.2025.100292>

Received 23 October 2024; Received in revised form 17 January 2025; Accepted 31 January 2025

Available online 15 February 2025

2666-3309/© 2025 The Author(s). Published by Elsevier B.V. This is an open access article under the CC BY license (<http://creativecommons.org/licenses/by/4.0/>).

However, the use of PAW increases the manufacturing time and affects the scalability. Though GMAW offers lower geometrical accuracy than GTAW and PAW, GMAW offers distinct advantages in terms of deposition rates (Wu et al., 2018).

The layer-by-layer deposition sequence in WAAM makes it possible to obtain tailored properties required for specific applications, i.e. properties on demand. Tailoring material properties using WAAM leads to better material performance with the potential to increase strength, toughness, hardness or resistance to corrosion. Hitherto, tailored properties in parts fabricated with WAAM have been achieved by the use of process parameter modulation (GMAW, CMT etc.) (Panchenko et al., 2022; Müller et al., 2019; Rodrigues et al., 2019; Fang et al., 2022; Henckell et al., 2020; Yildiz et al., 2020), compositional control (Chandrasekaran et al., 2020; Wu et al., 2020; Ahsan et al., 2021, 2020; Rodrigues et al., 2020) or in-situ thermo-mechanical treatments (Donoghue et al., 2016; Scotti et al., 2020; da Silva et al., 2020).

In addition to WAAM process parameter modulation (Yildiz et al., 2020; Müller et al., 2019; Rodrigues et al., 2019; Fang et al., 2022; Henckell et al., 2020), preheating and interpass temperatures (Vahedi Nemani et al., 2021; Zhai et al., 2022) also affect the microstructure development and thus the mechanical properties. Appropriate process parameter selection plays a vital role in the geometrical accuracy of constructed parts. Geometrical accuracy has an influence on the amount of material to be machined and on the material properties. Poor geometrical features that function as stress concentration points or sites for initiating fracture can contribute to the degradation of material properties. It is crucial to comprehend how processing conditions, geometry, microstructure and properties are interconnected to achieve precise control over local properties while minimizing deviations from the intended design geometry.

With good weldability and strength properties, high-strength low alloy steels (HSLA) are a good choice for marine, offshore and structural applications. This has led to widespread research on WAAM of high strength low alloy (HSLA) steels which can be classified either as normal strength (< 600 MPa) or high strength steels (> 700 MPa) based on their tensile strength (Huang et al., 2023). Solid-state phase transformations in HSLA steels facilitate the tuning of material properties by controlling the phase fractions of ferrite, bainite and martensite; hence, control over process parameters is necessary to ensure that these solid-state phase transformations are optimized for desired properties. Several normal strength and high strength steel grades have been used in WAAM deposition including *ER70S-G* (Haden et al., 2017; Müller et al., 2019; Rafieezad et al., 2019; Ghaffari et al., 2019), *ER90S-B* (Dirisu et al., 2019), *ER100S* (Bourlet et al., 2020; Ermakova et al., 2020), *ER110S-G* (Rodrigues et al., 2019; Duarte et al., 2021; Mishra et al., 2023; Babu et al., 2023) and *ER120S-G* (Dirisu et al., 2019). Several authors studied the microstructure and properties of a single HSLA steel wall or blocks printed with optimized parameters demonstrating low defect occurrence and comparable mechanical properties to the wrought material (Nemani et al., 2020; Ghaffari et al., 2019). The primary focus of these studies was directed towards elucidating either the local microstructure variation (Sun et al., 2020a) or the anisotropy of material properties in different directions (Dirisu et al., 2019; Chen et al., 2024). Rodrigues et al. (2019) fabricated thin walls with low and high heat input to study the effect of heat input on *ER110S-G* steel. Furthermore, Duarte et al. (2021) linked heat input measured during continuous deposition and synergic pulsed deposition to geometry, microstructure and mechanical properties of high-strength steel. An increase in the yield strength and ultimate tensile strength (UTS) of the material was observed with low heat input in both studies mentioned above (Rodrigues et al., 2019; Duarte et al., 2021). A few other studies on WAAM of high-strength steels (HSS) have focused on the effect of deposition strategies on microstructure and mechanical properties of rectangular blocks (Aldalur et al., 2020; Dirisu et al., 2019; Xu et al., 2019). These studies linked thermal accumulation

Table 1

Process parameters used for the fabrication of the thin walls.

Specimen #	Wire Feed Rate (m/min)	Travel Speed (mm/s)
S1	6	5
S2	6	7.5
S3	6	10
S4	6	14
S5	6	17
S6	2	10
S7	4	10
S8	8	10
S9	10	10

during weaving or oscillation deposition strategies to deterioration in mechanical properties such as strength and hardness when compared to blocks fabricated with parallel deposition.

Most of the previous studies on *ER110S-G* steel dealt with the use of an optimum process parameter for deposition (Mishra et al., 2023; Rodrigues et al., 2019; Duarte et al., 2021) or a limited range of heat input was considered (Rodrigues et al., 2019; Duarte et al., 2021). Heat input is dependent on several other process variables such as wire feed rate, travel speed, contact tip to workpiece distance, shielding gas etc. Similar heat inputs can be obtained through different combinations of these parameters. Among these, wire feed rate and travel speed are crucial parameters that can be easily altered and that directly impact the amount of heat input into the manufactured component. Hence, a systematic study is necessary to correlate wire feed rate and travel speed with geometry, microstructure and mechanical properties. In the present study, a wide range of parameters is considered with heat inputs ranging from approximately 178 J/mm to 982 J/mm by altering wire feed rate and travel speed. During processing real-time thermal measurements were conducted to correlate process parameters to microstructure. A systematic experimental approach is undertaken to understand the influence of WAAM process parameters on the geometry, microstructure and properties. A simple rectangular thin wall was chosen as the geometry for the study. Thin walls are fabricated, keeping travel speed constant and varying wire feed rate and vice versa. Thermal field evaluation was performed on these depositions with a thermal camera. Thermographs and average cooling rates were obtained from real-time thermal measurements and correlated to the observed microstructure of the samples. Geometrical features such as height, effective width and surface waviness of each sample were also measured. Finally, tensile tests and microhardness measurements were made to better understand the influence of process parameters on the microstructure and properties of the deposited material.

Experimental methodology

Experimental setup and sample deposition

Multi-layer thin walls with 30 layers and 200 mm lengths were deposited with different processing parameters using a CMT-5000i power source integrated with a Fanuc 6-axis robot. Pulsed mode deposition was used with a contact tip to workpiece distance of 15 mm. Walls were deposited bidirectionally to maintain a constant height (Dehaghani et al., 2023). The process parameters used for the deposition of each wall are listed in Table 1.

Protegon (85%Ar + 15%CO₂) was used as shielding gas at a flow rate of 17 l/min. Interpass temperature between the deposition of subsequent layers was maintained at 150 °C. The walls were deposited on a high-strength steel S690 grade substrate of 250 × 140 × 25 mm³. A high-strength steel wire (AWS A5.28: ER110S-G) of 1.2 mm diameter (Lincoln Electric) was used as the feedstock. The nominal composition of the wire is given in Table 2.

Table 2
Composition of high strength steel wire (LNMoNiVa) as provided by the supplier.

Element	C	Mn	Ni	Si	Cr	Mo	Cu	V	Fe
Weight percentage	0.09	1.7	1.4	0.54	0.3	0.24	0.06	0.08	Balance

Process evaluation methods

Current and voltage characteristics of the deposition were measured at 5 kHz with Triton 4000 data logger. Heat input is estimated from the instantaneous voltage (V_i), current (I_i) and travel speed (TS) (Mishra et al., 2023). Linear heat input (HI) in the WAAM process is defined by the relationship given in Eq. (1) taking the process efficiency (η) value of 0.8 into account (Sun et al., 2020c).

$$HI = \frac{\eta \sum_{i=0}^n \frac{V_i I_i}{n}}{TS}, \quad (1)$$

where η is the process efficiency and n is the number of measurements. An infrared camera (Infratec VarioCAM HD) was used to evaluate the thermal field corresponding to multiple bead depositions. The thermal field evaluation was focused specifically on extracting the cooling rates observed between 800 °C and 500 °C, as well as the evolution of the heat-affected zone within the temperature range of 1200 °C and 800 °C, which corresponds to the solid phase. A constant emissivity value of 0.92 obtained from previous literature was used to evaluate the thermal field (Behrooz, 2020) after solidification. Since a protective glass window was used to shield the thermal camera from weld spatters, the window's transmissivity is also considered in the temperature field estimation.

Geometrical characterization

After the deposition of each layer, layer height was measured at three locations within the sample using a vernier calliper. Height measurements were performed ensuring that the measurement points were not located in the start or stop region of the deposit. The maximum width and effective width correspond to peaks and valleys within a specific region in the transverse cross-section extracted from the centre along the length of the wall as indicated in Fig. 1. Surface waviness is related to the maximum distance between the peak and the valley in a given area of the deposited wall and was estimated using the method described by Geng et al. (2018). A transverse cross-section image of the wall was divided into five regions of equal length excluding the top bead and bottom beads as indicated in Fig. 1. Measurements of the maximum width and effective width were obtained from each of the five regions of the transverse cross-section images using the image processing software ImageJ. Then, the surface waviness (SW) of each region from the fabricated sample was obtained using Eq. (2).

$$SW = \frac{MW - EW}{2} \quad (2)$$

where MW is the maximum width and EW is the effective width of each region. The average surface waviness of a sample was obtained from the surface waviness values of the five regions corresponding to a sample.

Microstructural characterization

Transverse cross-sections were extracted from the thin-walled samples for microstructural characterization. Standard metallographic preparation procedures were applied on the samples, which included mounting, grinding and polishing. Chemical etching of the polished sample was performed with a Nital 2% solution to reveal the microstructure. An Olympus BXM60 and a Keyence VHX-5000 digital microscope were employed to obtain optical micrographs and macrographs from the transverse cross-sections. Scanning electron micrographs were obtained using a Jeol JSM-IT200 InTouch Scope and a

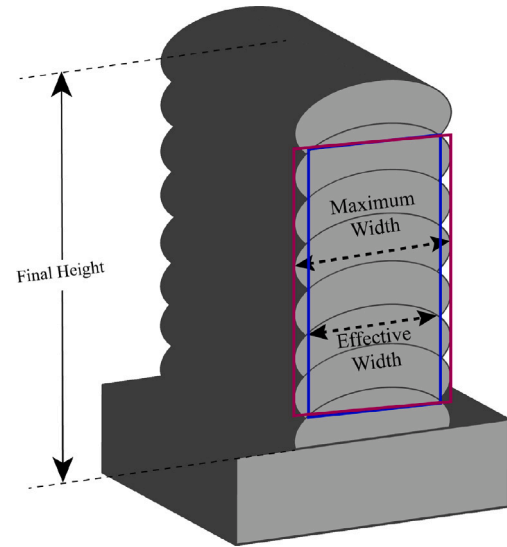


Fig. 1. Schematic illustration of the geometrical feature measurements.

Jeol 6500F-field emission gun SEM. Phase analysis to estimate retained austenite in the middle section of the wall samples was achieved by XRD with a $\text{CuK}\alpha$ target and a step size of 0.040° for a measuring time of 2 s. Samples for EBSD measurements were subjected to OPS polishing for 40 min in addition to the previously mentioned sample preparation methods. All EBSD measurements were conducted on the transverse cross-section of thin walls, focusing on the fusion zone corresponding to the 15th layer of the wall samples. EBSD measurements were performed using a Thermo Scientific™ Helios™ G4 PFIB UXe SEM equipped with an EDAX detector. A step size of $0.25 \mu\text{m}$ was used. TSL OIM Analysis 8 software was used to analyse the measured data.

Mechanical property evaluation

Microhardness measurements were performed in accordance with ASTM E92-23 on the transverse cross-section of the extracted samples parallel to the build direction with a Struers Durascan hardness tester. A load of 1 kg was used with a holding time of 15 s. Determination of further mechanical properties of the sample was accomplished with tensile testing of specimens extracted from the thin walls at room temperature. Six specimens were extracted from each wall of which three were oriented horizontally i.e. parallel to the deposition direction (DD) and the other three were oriented vertically i.e. parallel to the building direction (BD). Due to the limitations associated with the height of walls a non-standard specimen was used for the tensile testing. A schematic of sample locations and tensile specimen dimensions (Fu et al., 2019) is given in Fig. 2. An Instron 5500 universal testing machine was used for tensile testing with a cross-head displacement of 4.5 mm/min. The displacement during testing was measured using an extensometer with a gauge length of 10 mm. The ultimate tensile strength and total elongation at fracture of the samples were obtained from the resultant stress-strain curves conforming to ASTM E8 standards.

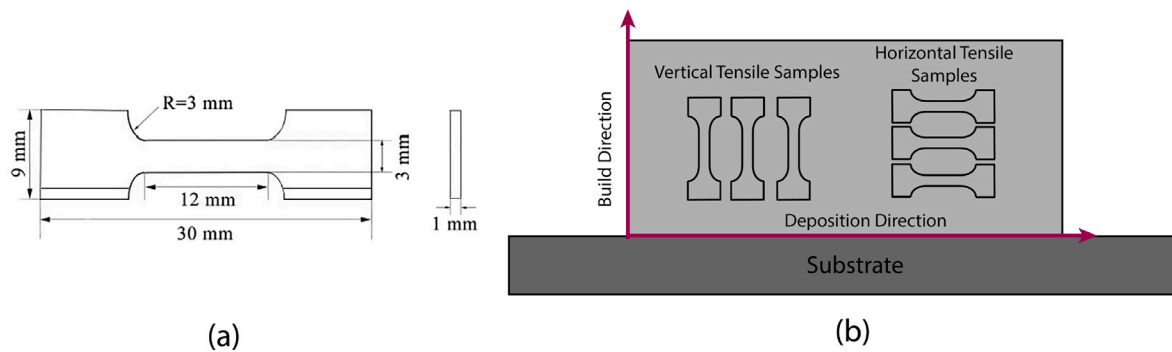


Fig. 2. (a) Tensile specimen dimensions in tensile testing. (b) Schematic of tensile sample location from each wall.

Table 3

Average current, voltage and frequency obtained from the current–voltage characteristics acquired during the fabrication of thin wall structures.

Sample #	Wire feed rate (m/min)	Travel speed (mm/s)	Average current (A)	Average voltage (V)	Average pulse frequency (Hz)	Instantaneous heat input (J/mm)
S1	6	5	145	24	127	982
S2	6	7.5	152	24	132	690
S3	6	10	157	24	135	545
S4	6	13.5	141	24	125	384
S5	6	17	134	24	122	307
S6	2	10	57	19	55	178
S7	4	10	88	22	80	314
S8	8	10	202	28	175	702
S9	10	10	256	30	208	966

Result and discussion

Current and voltage characteristics

The average current (I_{avg}), average voltage (V_{avg}) and pulse frequency obtained during the process is given in Table 3. Due to the use of synergic pulsed GMAW I_{avg} , V_{avg} and pulse frequency is only affected by an increase in the wire feed rate. When the wire feed rate is ramped up in synergic pulsed GMAW, the power source is designed to increase welding power to melt the wire electrode automatically. However, to increase welding power the optimal pulse frequency is also increased to prevent overheating of the deposit and distortion.

The current–voltage characteristics of the thin wall structures deposited with different wire feed rates are given in Fig. 3. It can be observed that pulse duration and background current both displayed an increasing trend when the wire feed rate is increased. A high background current maintains the arc during the base period and helps in maintaining the arc stability to enable smooth droplet transfer and hence lower spatter. In the case of a wire feed rate of 10 m/min, a background current of approximately 100 A is observed. Such high background currents are associated with a high droplet transfer rate facilitating a higher deposition rate (Pal and Pal, 2011). High background current can cause the overall heat input to increase due to higher average current and heat transfer to the workpiece. It can be inferred from Fig. 3 that a relatively higher peak current and lower peak duration are observed for the wire feed rates of 2 m/min and 6 m/min. The combined effect of high peak current with short peak duration can result in a short melt pool and higher droplet velocities. This enables the droplet to enter the melt pool overcoming the surface tension, reducing the spatter and promoting better fusion. Hence better surface quality can be expected in samples with wire feed rates less than or about 6 m/min.

From measured instantaneous voltage and current data in combination with selected travel speed, the linear heat input is calculated with a process efficiency of 0.8 (Norrish, 2017) according to Eq. (1) for the samples listed in Table 1. The heat input as a function of travel speed and wire feed rate is displayed in Fig. 4. Travel speed has an inverse relationship with the heat input as indicated in Eq. (1). A synergic

welding mode was used for the deposition due to which the wire feed rate is proportional to the average current and also voltage; hence, heat input is directly proportional to the wire feed rate used.

Geometry

The influence of wire feed rate and travel speed on the total height and effective width of the deposits are given in Figs. 5 and 6, respectively.

Increasing the wire feed rate or decreasing the travel speed results in a higher total height, individual layer height and effective width of the samples. Samples with higher wire feed rates have higher height and wider beads due to the increased material deposition per unit length. Reducing travel speeds results in an increased time per unit length of the deposition trajectory also resulting in higher material deposition.

It was observed that sample S1 has a greater final height and lower maximum width and surface waviness than sample S9 even though heat inputs (Fig. 4) are similar. Samples deposited with high wire feed rates like S9 have a high welding current and voltage (Table 3). An increase in the welding current and voltage leads to an increase in arc pressure and heat flow to the material leading to the superheating of the deposited droplets. Higher arc pressure, along with the high heat content of the sample, tends to push the liquid metal to the outer peripheries. High pulse frequency associated with sample S9 leads to shorter pulse duration. A shorter pulse duration combined with high average current ensures that the weld remains molten when additional wire material is added to the melt pool during the next pulse. Successive welding pulses exert arc pressure over the liquid melt pool, forcing molten metal to spread out and widen, resulting in lower bead height and wider beads.

Surface waviness is a critical parameter in WAAM deposition, as it is directly linked to the volume of material that needs to be machined to obtain a smooth surface finish. Qualitative and quantitative comparisons of the surface waviness of the samples are indicated in Fig. 5 (e) (f) and Fig. 6. Samples fabricated with a higher heat input (S9) have a higher surface waviness. This is due to the increased volume of molten metal associated with a high wire feed rate combined with a higher frequency of pulsed arc pressure during pulsed GMAW which can result

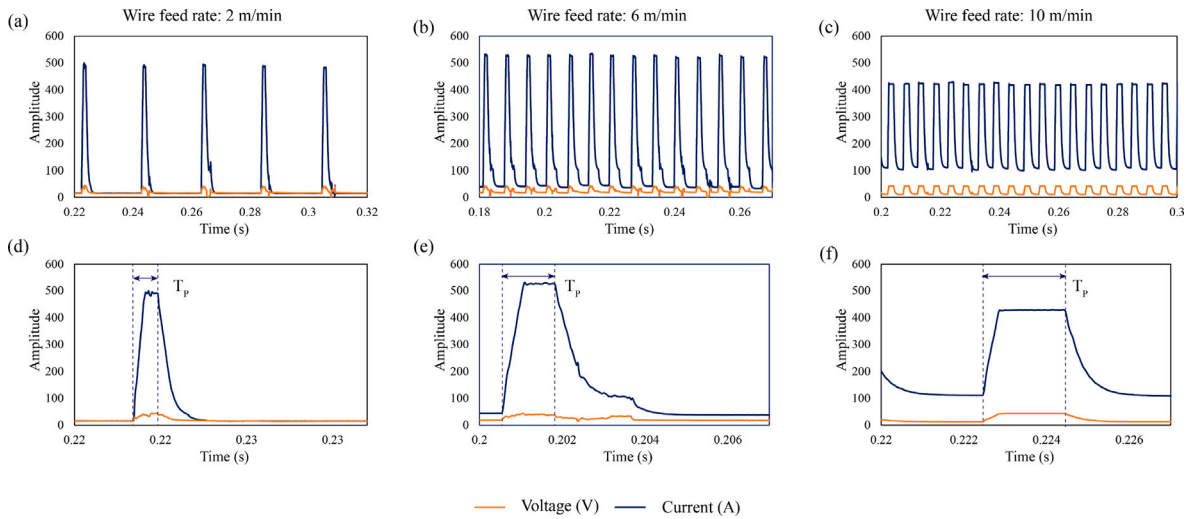


Fig. 3. Current voltage characteristics of samples deposited with increasing wire feed rate and constant travel speed (a) & (d) 2 m/min, (b) & (e) 6 m/min and (c) & (f) 10 m/min.

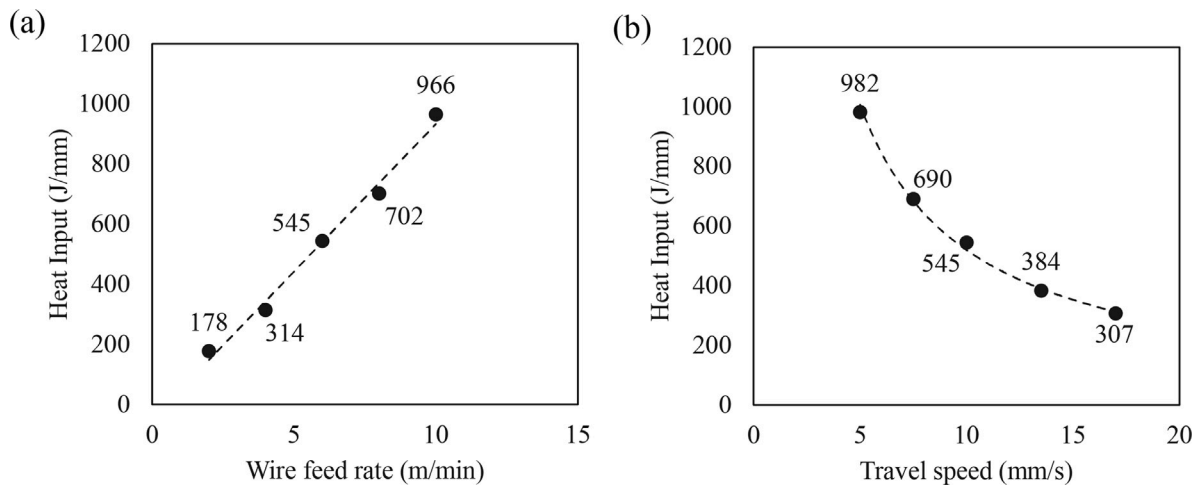


Fig. 4. Variation of heat input with (a) wire feed rate at a constant travel speed of 10 mm/s and (b) travel speed at a constant wire feed rate of 6 m/min. For a detailed discussion on the temperature effects of heat input refer to Section “Cooling rate analysis”.

in the spreading of the molten weld pool. It should be noted that the surface waviness of sample S5 is much higher than that of sample S6, even though sample S6 has a lower heat input. This is related to the humping defect observed in sample S5. The humping defect is characterized by the occurrence of peaks and troughs periodically along the welding direction (Norrish et al., 2021). Previous studies have linked humping to a Kelvin–Helmholtz hydrodynamic instability caused by the relative motion of surface waves opposite to the welding direction (Kumar and DebRoy, 2006) or when the weld pool length exceeds a critical value (Bradstreet, 1968). The variations in height along the weld bead result in changes in contact tip-to-workpiece (CTWD) distance and resultant heat input. The instabilities caused by these variations lead to surface undulations along the deposition direction and the plane parallel to both the deposition direction and build direction, as indicated in Fig. 6. Though S1 and S9 samples were deposited with similar heat input, sample S9 has a higher surface waviness than S1. Higher background current and deposition frequency in S9 instigate the formation of wider beads and thermal distortions. Therefore, to achieve higher deposition rates for faster production or thicker single bead walls (thickness > 8 mm), using lower travel speeds rather than higher wire feed rates promotes geometrical accuracy and lowers the amount of machining required to achieve the required thickness. Similarly, when aiming for reduced heat input or thin single

bead walls (thickness < 5 mm), opting for a lower wire feed rate rather than higher travel speeds is recommended for creating a more near-net-shaped part.

Cooling rate analysis

Thermal field measurements of the WAAM process help to elucidate the microstructural evolution during the deposition process. Metallurgical phenomena including solidification, solid-state phase transformation and tempering govern the final microstructure of WAAM-deposited S690 grade high-strength steel.

In carbon steels, phase composition is one of the most critical microstructural aspects affecting final mechanical properties. Generally, high-strength steel microstructures comprise a mixture of different ferrite morphologies and martensite (Mishra et al., 2023). Cooling rates experienced by the material while cooling down from the austenitization temperature determine the fraction of constituents (Bhadeshia and Honeycombe, 2017). From the measured thermal profiles the time taken by the material to cool from 800 °C to 500 °C ($t_{8/5}$) can be evaluated. The estimated $t_{8/5}$ is used to calculate the average cooling rate, which is linked to the solid-state phase transformation in steels (Bhadeshia and Honeycombe, 2017).

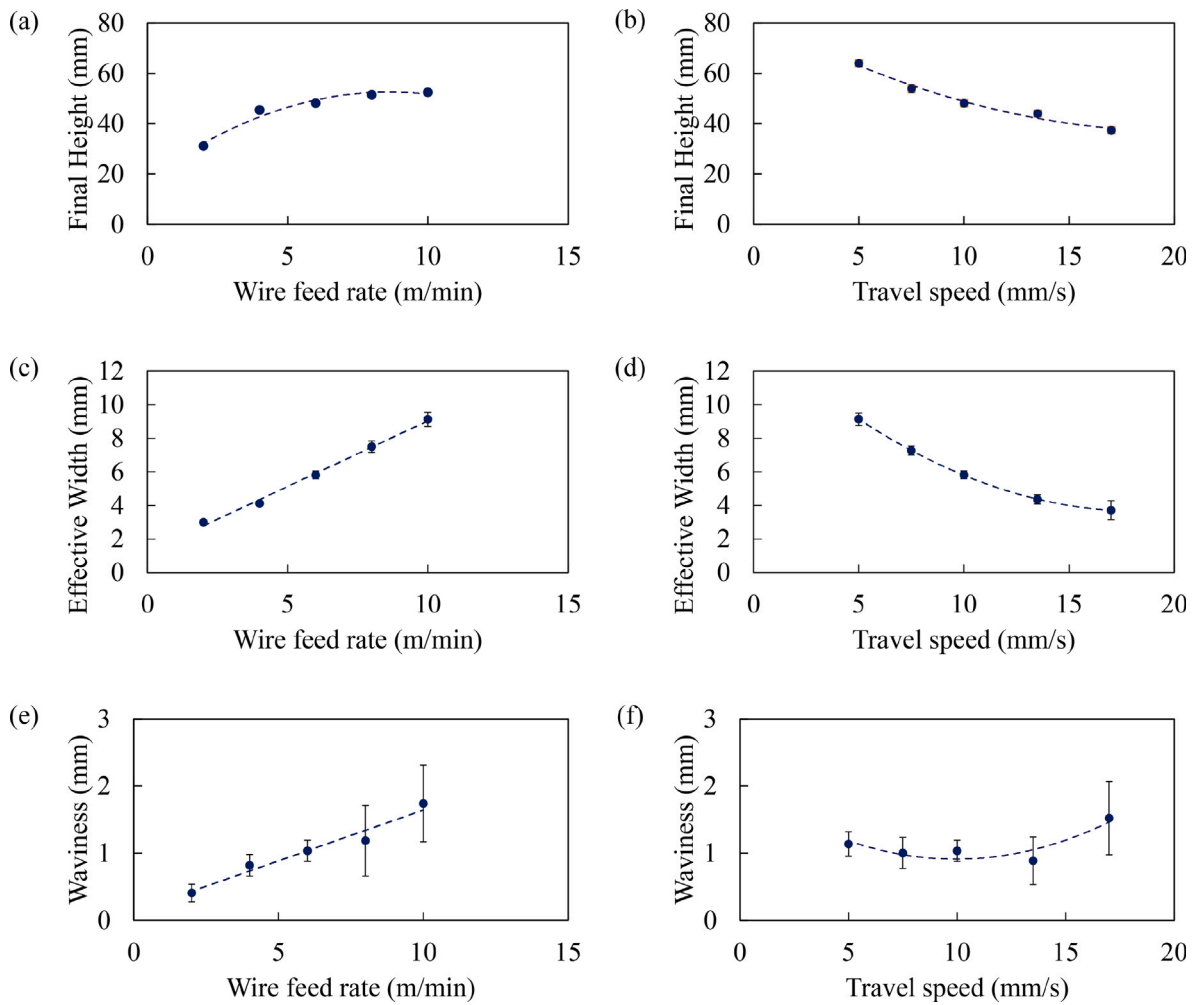


Fig. 5. Variation of final height (a,b), effective width (c,d) and surface waviness (e,f) with changing wire feed rate (at constant TS = 10 mm/s) and travel speed (at constant WFR = 6 m/min).

The thermal profile at a material point in the 15th layer during the WAAM deposition of a thin wall is indicated in Fig. 7. We refer to the thermal cycle experienced by a material point in a bead during deposition as the solidification thermal cycle when the peak bead temperatures exceed the melting temperature ($T > T_{Melting}$). The solidification thermal cycle influences grain size and distribution in the deposited material. The cooling rates extracted from the solidification thermal cycle of samples deposited with different heat input indicates how cooling rates evolve along the build direction when the heat input is varied. Fig. 8(a) indicates the cooling rate evolution and thermal accumulation along the height of the samples deposited with different heat inputs. Higher cooling rates are observed close to the substrate plate for all the samples. However, a substantial difference of approximately 150 °C/s in the cooling rates was observed between the samples deposited with the highest and lowest heat inputs. As the layer height increases, the cooling rates decrease. For samples S3 and S1, the cooling rates reach almost a uniform value indicating a steady-state thermal condition. This can also be noted from the thermographs displayed in Fig. 8 where the heat-affected zone appears to have similar dimensions in the case of the 15th layer and the 25th layer. For sample S6, since the heat input is low, cooling rates display a decreasing trend even for the 30th layer. It is reasonable to anticipate that adding more layers can result in attaining a uniform cooling rate. Low cooling rates along the build direction are experienced due to lower heat flux to the base plate. This is caused by the reduction in thermal gradient due to thermal accumulation by subsequent bead depositions. As a result, the heat-affected zone (HAZ) region is more prominent in 15th and 25th layers in

all cases. From Fig. 8, it can be observed that for sample S3, uniform cooling rates are achieved after the 10th layer. This aligns with similar heat-affected zones observed in Figs. 8(d) and 8(e). Qualitatively, it can be inferred that the heat-affected zone increases in size with the deposition of each bead until stable thermal conditions are reached, at which point the size remains consistent.

Cooling rates (between 800 °C and 500 °C) calculated for the critical thermal cycle with a peak temperature above A_{c3} as indicated in Fig. 7 are presented in Fig. 9. The A_{c3} critical temperature for austenitization for the ER110S-G High Strength Steel is 804 °C, based on equilibrium calculations performed with Thermocalc. Cooling rates corresponding to the critical thermal cycle at the 5th, 15th and 25th layers of all samples deposited with varying wire feed rates and travel speeds are given in Fig. 9. For all the cases, it can be observed that cooling rates in the 5th layer are higher than in the 15th and the 25th layers. The high cooling rates in lower layers are caused by greater thermal conduction to the substrate. In the 5th layer, for a wire feed rate of 2 m/min, the cooling rate is as high as 80 °C/s. This is close to the critical cooling rate for complete martensite transformation for the high-strength steel composition used. High cooling rates observed in samples deposited with a low wire feed rate of 2 m/min are related to the relatively low heat input of 178 J/mm used for this sample. Variations in the heat-affected zones observed in the 25th layer of the deposited walls and the final printed walls corresponding to different process parameters are given in Fig. 10. Lower heat input leads to lower thermal accumulation in samples deposited with a wire feed rate of 2 m/min, which can

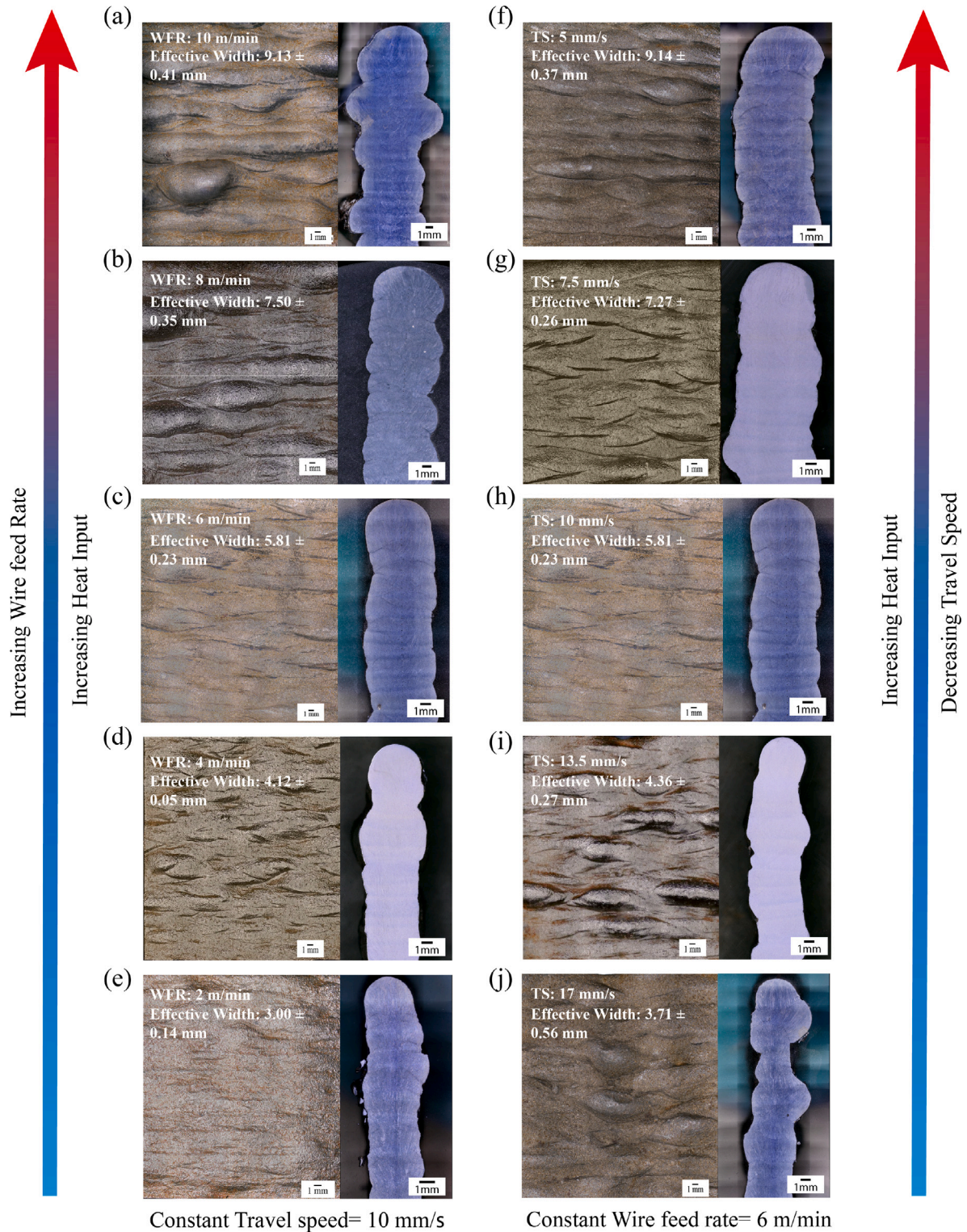


Fig. 6. Qualitative evaluation of surface waviness corresponding to side view and cross-sectional view of samples deposited with varying wire feed rate (at constant TS = 10 mm/s) and travel speed (at constant WFR = 6 m/min).

also be evidenced by a relatively smaller heat-affected zone indicated in Fig. 10(a). As the layer height increases, the cooling rates drop to approximately 40 °C/s for the 15th and 25th layer. However, for a high wire feed rate of 10 m/min, the 5th layer has a cooling rate of approximately 20 °C/s, much less than in the case of a wire feed rate of 2 m/min. Cooling rates in 15th and 25th layer for sample S9 drop to

much lower values of 8 °C/s and 7 °C/s, respectively. A similar trend can also be observed when the travel speed is varied.

Simultaneous increase of wire feed rate and decrease of travel speed leads to lower cooling rates in all the layers due to the increased heat input into the samples. High heat input causes thermal accumulation in the samples resulting in lower thermal gradients within the sample.

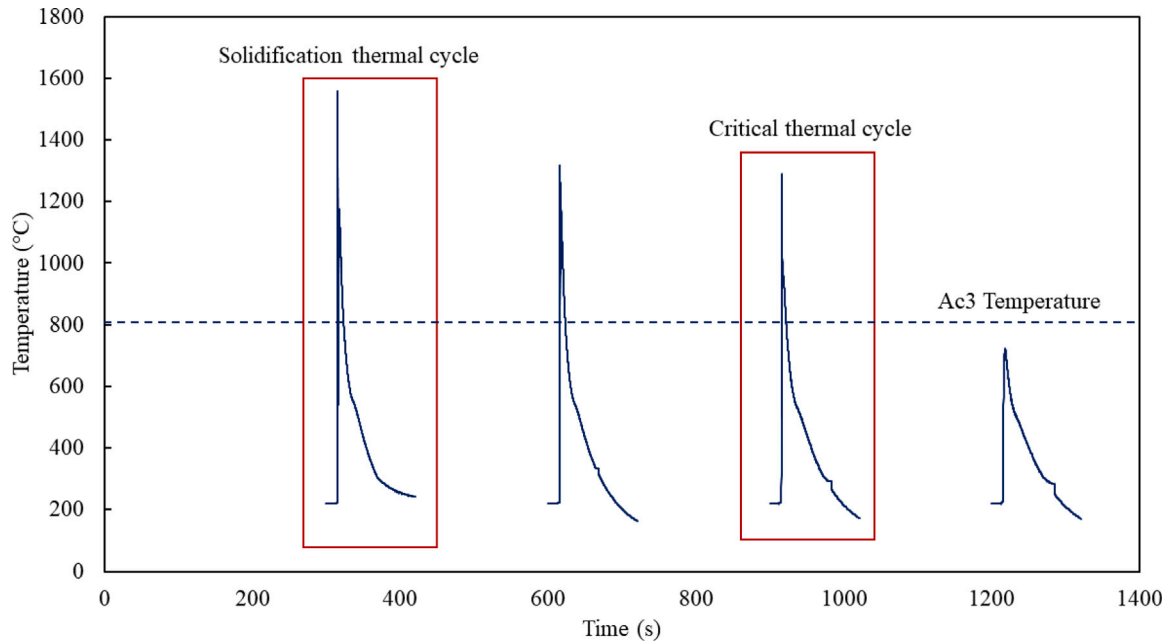


Fig. 7. Thermal profile obtained from the centre point of the 15th layer indicating the solidification thermal cycle and the critical thermal cycle during WAAM.

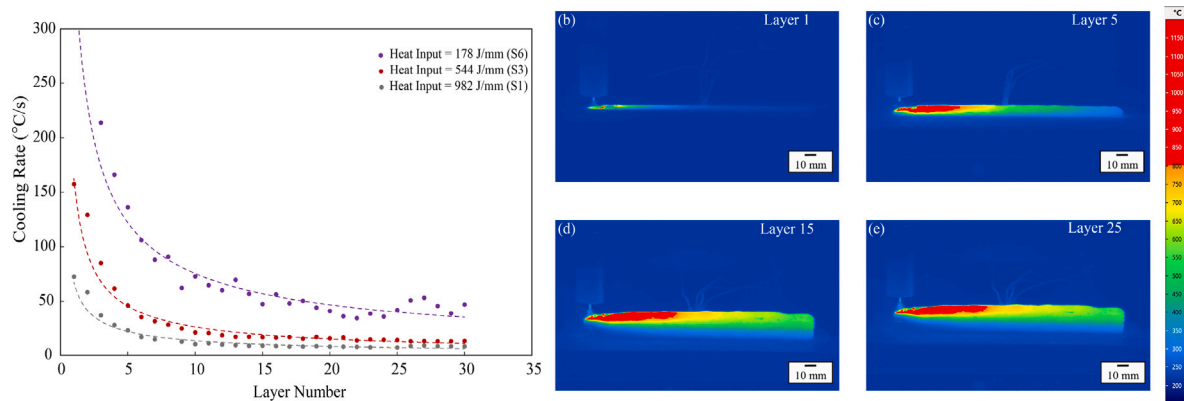


Fig. 8. (a) Cooling rates obtained from the solidification thermal cycle experienced by each bead during WAAM (b),(c), (d) and (e) indicate the thermographs for different layers obtained from sample S3 deposited with a heat input of 544 J/mm (Wire feed rate = 6 m/min and Travel speed = 10 mm/s). The region marked with red indicates the regions heated to temperatures above the A_{C3} temperature.

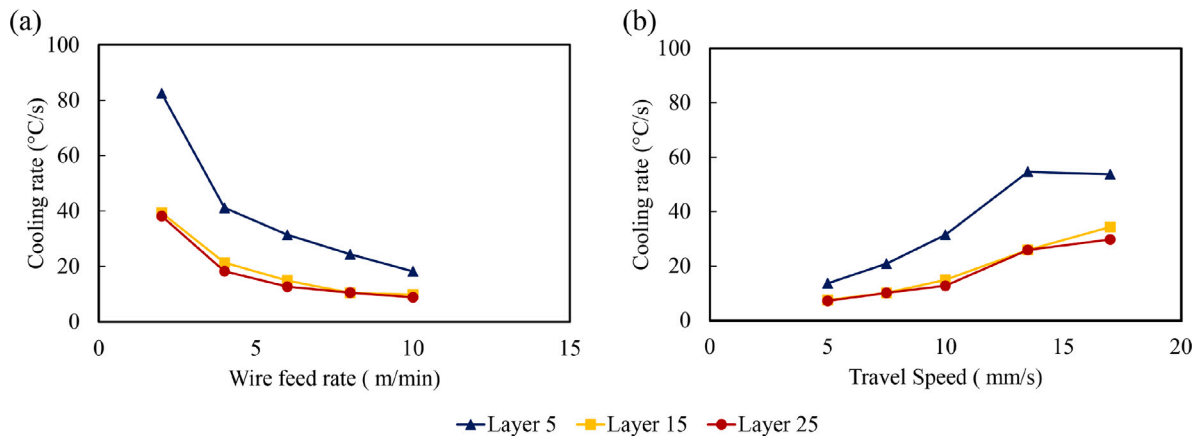


Fig. 9. Average Cooling rate estimated from critical cooling cycles corresponding to thin walls fabricated with (a) varying wire feed rate (at constant TS = 10 mm/s) and (b) varying travel speed (at constant WFR = 6 m/min).

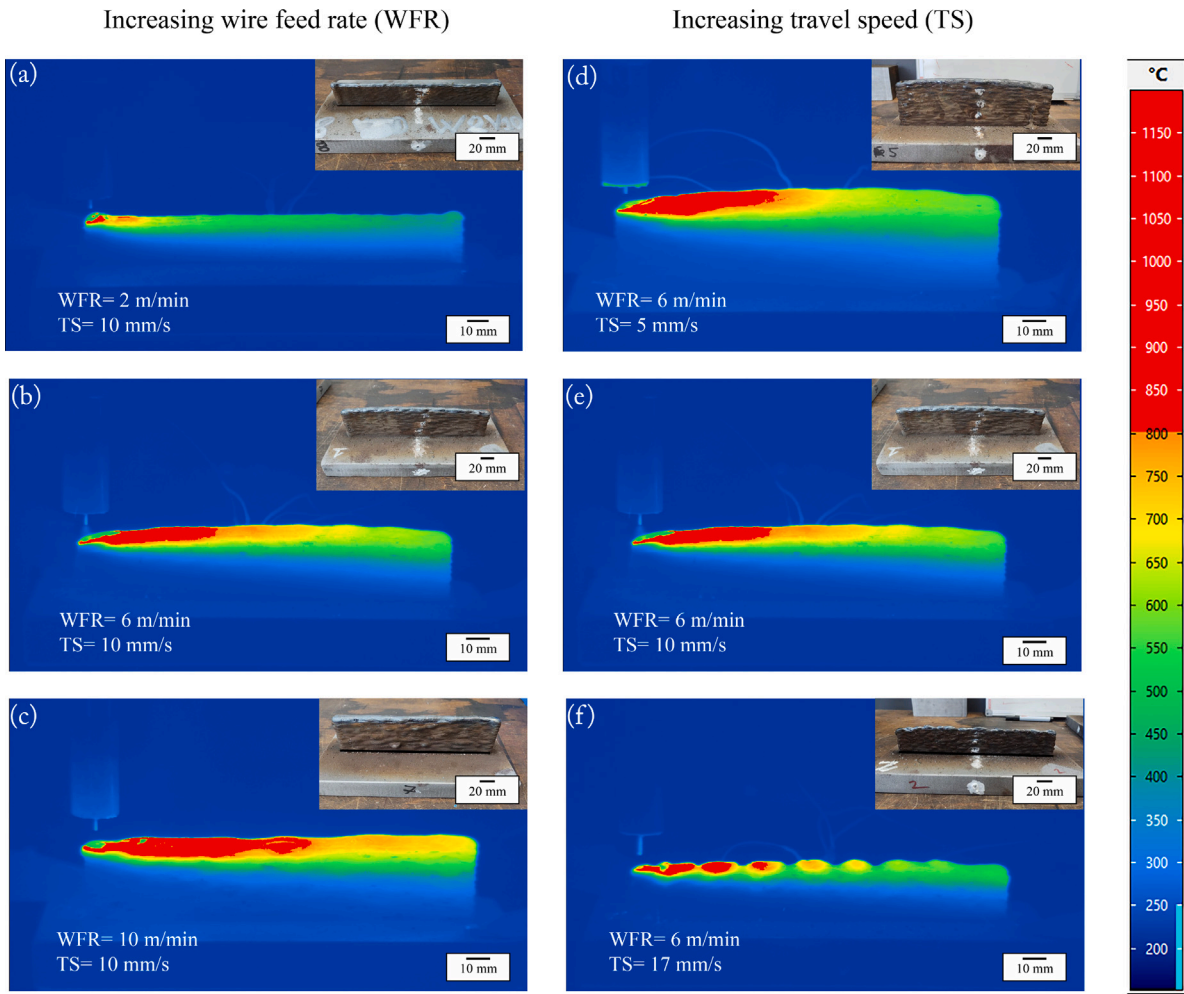


Fig. 10. Thermographs extracted from thermal camera measurements on 25th layer of samples deposited with varying process parameters. The region marked red in the thermographs indicates the heat-affected zone ($T > T_{Ac3}$) corresponding to each deposition. Insets in each sub figure indicates the final printed wall corresponding to each thermograph.

Samples with the lowest travel speed (S1) and highest wire feed rate (S9) have larger heat-affected zones due to increased heat accumulation which reduces the cooling rates as indicated in Fig. 10.

When the wire feed rate is reduced to a level where the heat input is as low as 178 J/mm, we observe cooling rates of approximately 40 °C/s even in the 25th layer. When the heat input exceeds 545 J/mm, altering the wire feed rate or travel speed results in comparable cooling rates in high-strength steels. Fewer microstructural variations are expected to be observed in these samples due to the similarity in cooling rates. Altering wire feed rate or travel speed while keeping one of them constant leads to similar trends in cooling rate observed in the deposited thin wall structures, it can therefore be concluded that the predominant influence on cooling rates is due to variation in the heat input.

Microstructure characterization

Different ferrite morphologies (Polygonal ferrite, Widmanstätten Ferrite, Acicular Ferrite and Upper Bainite) and Martensite are the most commonly found microstructural constituents in high-strength steel microstructures (Rodrigues et al., 2019; Thompson et al., 1990, 1996). Each of these microstructural constituents have a unique influence on the overall mechanical behaviour, hence qualitative or quantitative understanding of the presence of each of the constituents is important.

A continuous cooling transformation (CCT) diagram corresponding to ER110S-G steel is obtained from the dilatometry data extracted from

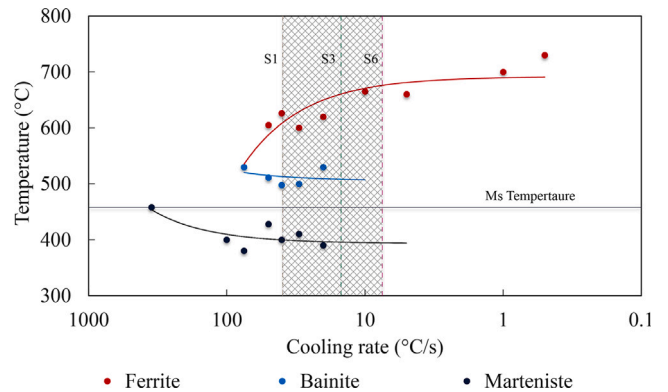


Fig. 11. CCT diagram of ER110S-G steel composition extracted from dilatometric data reported in our previous work (Mishra et al., 2023). The shaded region indicates the range of cooling rates measured from the 15th layer of all thin wall structures. The upper and lower bounds of the shaded region are indicated by the cooling rates of samples corresponding to samples deposited with the highest (S1) and lowest heat input (S6). (For interpretation of the references to colour in this figure legend, the reader is referred to the web version of this article.)

our previous study (Mishra et al., 2023). According to the CCT diagram, austenite transformation to a fully ferritic microstructure occurs at cooling rates lower than 10 °C/s. Bainite formation (upper bainite

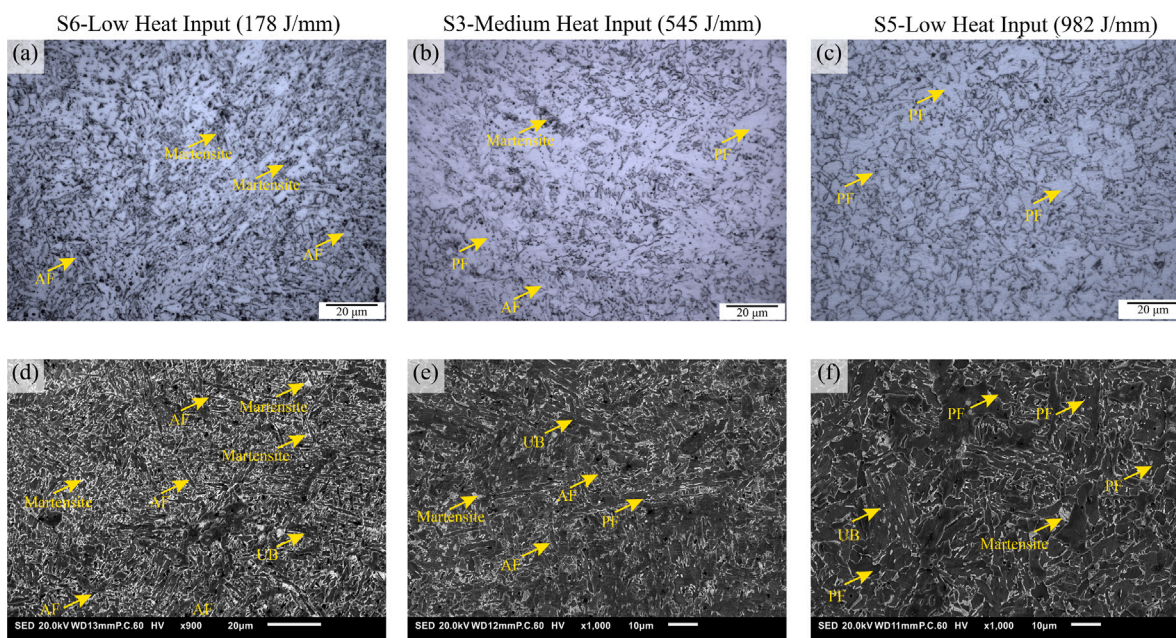


Fig. 12. (a-c) Optical and (d-f) Scanning electron micrographs extracted from the 10th bead of samples S6, S3 and S5 respectively.

and acicular ferrite) is observed between cooling rates of 20 °C/s and 75 °C/s. Above 75 °C/s, the material undergoes a fully martensitic transformation. Martensite formation is also observed in the case of cooling rates as low as 20 °C/s. However, this transformation happens at temperatures lower than the original martensite transformation start temperature. This is due to the carbon enrichment of the retained austenite after transformation to polygonal ferrite, acicular ferrite and bainite. The possible microstructures in the deposited samples can be derived by superimposing the cooling rates observed at the 15th layer of samples with high, medium and low heat inputs. Based on Figs. 9 and 11, sample S1 is expected to have a predominantly ferritic microstructure. Likewise, in sample S6, the bainite and martensite volume fractions are higher due to higher cooling rates.

Optical and scanning electron micrographs from samples deposited with different heat inputs indicate an apparent disparity as shown in Fig. 12. Samples with high heat input had a predominantly polygonal ferritic and granular bainitic microstructure. Also, the grain sizes are coarser in samples with higher heat input due to the grain growth of polygonal ferrite and granular bainite during slower cooling from the austenitic temperature range. In sample S3 with medium heat input, a mixed microstructure of polygonal ferrite, acicular ferrite, granular bainite and martensite is observed.

As the heat input decreases, cooling rates increase, promoting displacive transformation kinetics. This leads to more austenite undergoing displacive transformations producing a mixed microstructure of polygonal ferrite, bainite (upper bainite and acicular ferrite) and martensite. Hence, the fraction of martensite, bainite and acicular ferrite negatively correlates with heat input. Sample S6 possesses higher fractions of non-equilibrium constituents like bainite and martensite than S3 and S1. This is in accordance with the continuous cooling transformation (CCT) diagram indicated in Fig. 11.

Detailed microstructural quantification achieved through EBSD measurements illustrating the effect of heat input on the microstructure is given in Fig. 13. Kernel average misorientation (KAM) is the average misorientation between grains within a specified kernel size. Generally, KAM values correlate with dislocation density, i.e., higher KAM values indicate higher dislocation densities. Evaluation of the effect of heat

Table 4

Retained austenite fractions measured from the middle region of samples with different heat inputs.

Sample No	Heat input (J/mm)	Retained austenite fraction (%)
S6	178	2.9
S3	544	3.2
S5	985	2.9

input on KAM values reveals that average KAM values decrease from 0.76 to 0.66 as the heat input increases. This variation can be linked to the thermal field and associated phase transformations. Higher KAM values in S6 are caused by the higher cooling rates observed during deposition leading to the formation of non-equilibrium microstructural constituents with higher dislocation densities.

The percentage of high-angle grain boundaries (HAGBs) is also higher in the case of lower heat input samples. HAGBs are associated with prior austenite grain boundaries, acicular ferrite and martensite, whereas the low-angle grain boundaries are associated with coarse polygonal ferrite and lath boundaries. High-angle boundaries effectively impede dislocation motion and reduce plastic deformation, thus improving strength. High-angle grain boundaries also restrict crack propagation in materials. Hence, the higher HAGB fraction and average KAM values point towards higher strength for the thin walls with lower heat input (Fang et al., 2023).

Grain size plays a vital role in determining properties other than micro constituent fractions. Qualitative and quantitative evaluation of grain structure with EBSD reveals that lower heat input regions have a smaller grain size. Based on the Hall–Petch relationship, it is known that smaller grain size directly correlates with improved material strength (Sun et al., 2020b). In all samples, the maximum grain sizes were smaller than 30 μm. In sample S3 and sample S1, the grain sizes are relatively larger due to the formation of coarse polygonal ferrite and bainite due to the slower cooling rates during austenite decomposition. Additionally, grain sizes and their standard deviation are given in Fig. 13(i,j) and (k) corresponding to samples S6, S3 and S5 respectively. Higher standard deviation in grain sizes observed

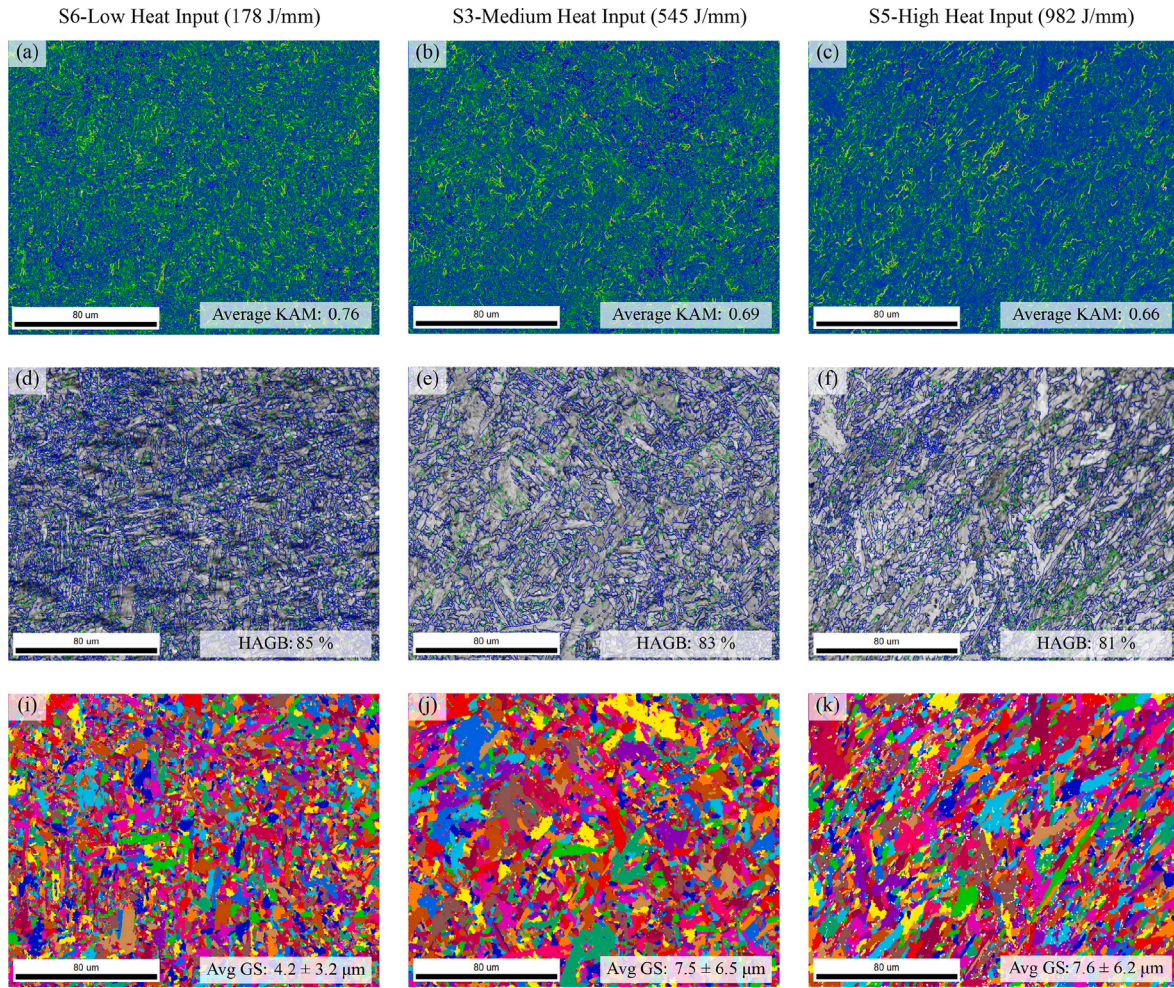


Fig. 13. EBSD characterization of the fusion zone corresponding to 15th layer of samples S6 (a, d, i), S3 (b, e, j), and S5 (c, f, k): (a–c) Kernel Average Misorientation (KAM) maps illustrating the local misorientation and strain distribution, (d–f) grain boundary distribution maps highlighting high-angle and low-angle boundaries and (i–k) grain size distribution maps showing the quantitative grain size analysis for each sample.

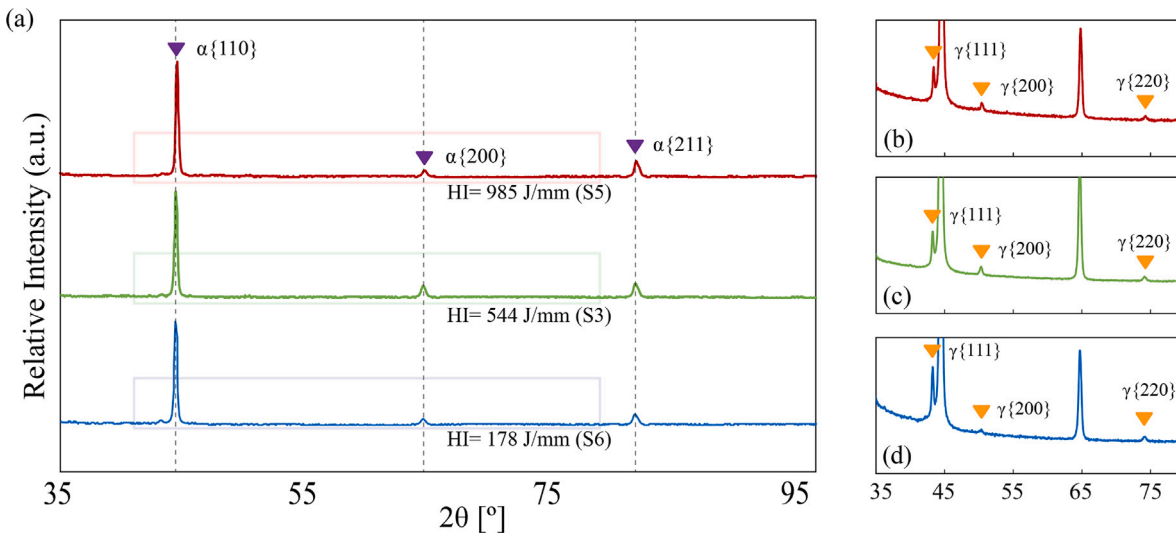


Fig. 14. (a) XRD patterns corresponding to samples deposited with different heat inputs. (b), (c) and (d) indicate the magnified region of XRD patterns indicating the austenite peaks.

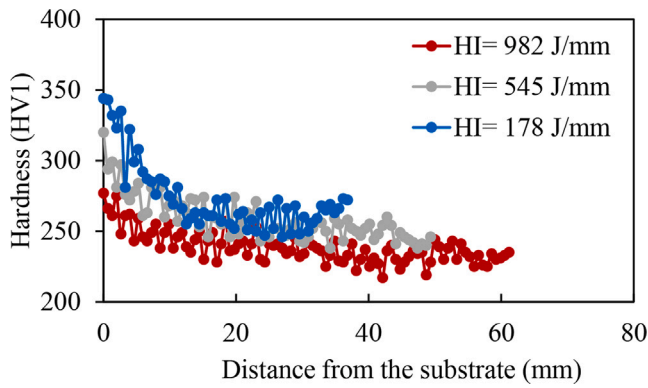


Fig. 15. Hardness along building direction for samples with varying heat input. The samples with varying heat input through control of travel speed also follow a similar trend.

in sample S3 and sample S5 indicates a relatively inhomogeneous distribution of grain sizes compared to sample S6.

XRD measurements on the samples with high, medium and low heat inputs shown in Fig. 14 indicated the presence of α ferrite with a BCC crystal structure confirmed by ferrite peaks of {110}, {200} and {211}. Nevertheless, retained austenite (RA) is also present, as indicated by the austenite peaks at {111}, {200}, and {220}. A comparison of retained austenite fractions estimated from XRD measurements is given in Table 4 showing no significant variation in retained austenite fraction with a change in heat input.

Mechanical property evaluation

Hardness measurements

Hardness distribution along the build direction for three heat inputs is presented in Fig. 15. A relatively higher hardness of around 340 HV can be observed in the first few layers of sample S6, owing to the higher cooling rates (substrate effect) as seen in Fig. 9. When heat input is increased, the hardness near the substrate decreases to 320 HV1 for sample S3 to 277 HV1 for sample S1. The hardness reduces as the layer height increases due to lower cooling rates. Between 20 mm and 30 mm height, the influence of heat dissipation through the substrate diminishes, leading to stable thermal conditions and uniform cooling rates. Referring to Fig. 9, for samples with varying heat inputs, the cooling rates observed at the 15th and 25th layers are below 40 °C/s. These cooling rates are characteristic of a ferritic microstructure with predominantly ferritic constituents and low fractions of martensite according to the CCT diagram given in Fig. 11. Due to the similar hardness of these ferritic microstructural constituents, the variation in cooling rates does not result in significant hardness variations along the build direction within this height range. Additionally, the material undergoes tempering due to subsequent thermal cycles between 20 mm and 30 mm. This leads to the softening of the martensite leading to a further reduction in the hardness of the material. Hence a combined effect of ferritic constituents and martensite tempering leads to similarity in hardness across the material between 20 mm and 30 mm (Mishra et al., 2023). An increase in hardness in the last deposited bead is observed as the material is subjected to only one thermal cycle; hence the occurrence of grain refinement and softening due to reheating and tempering does not occur.

The average hardness of each sample was estimated to understand the influence of process parameters on the hardness. Measurements were made excluding points from the first eight layers to avoid the substrate effect. For samples with increasing wire feed rates, it can be observed that samples S6 (2 m/min) and S9 (10 m/min) have a

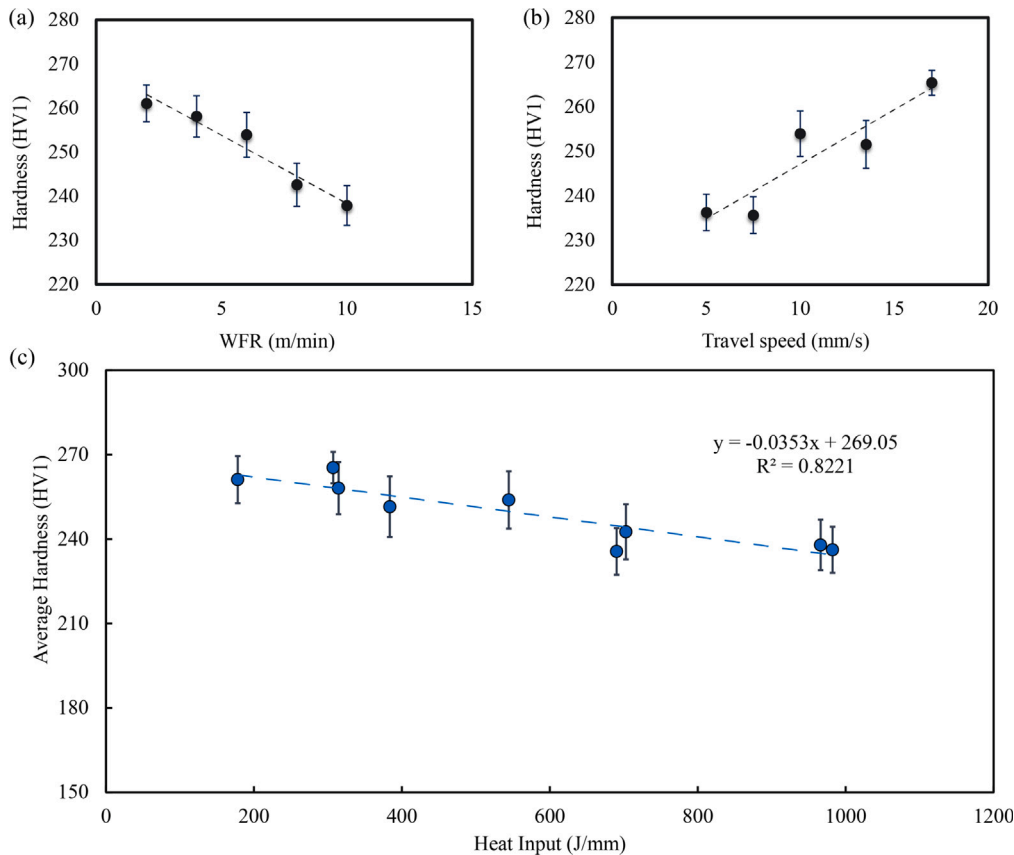


Fig. 16. Average hardness of samples deposited with (a) varying wire feed rate and (b) varying travel speed and (c) varying heat input.

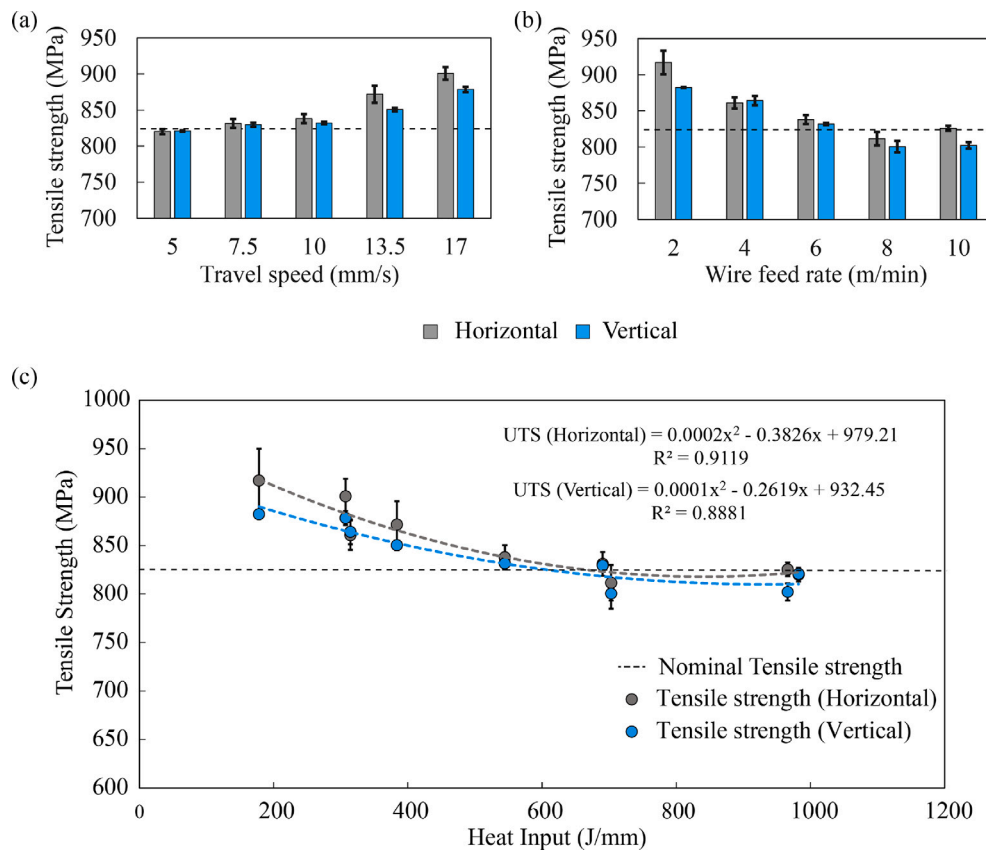


Fig. 17. Tensile strength of horizontally and vertically oriented samples with varying (a) wire feed rate and (b) travel speed (c) heat input. The nominal tensile strength is also indicated for comparison.

hardness of 261 HV and 237 HV, respectively. The hardness in samples with varying travel speeds varied from 265 HV in S5 to 236 HV in S1. This variation in hardness is related to the individual solid-state phase constituents observed in these samples. Martensite possesses higher hardness than other ferrite morphologies like bainite and ferrite. Based on the micrographs observed in Fig. 12, it is clear that samples S5 and S6 have higher fractions of martensite due to the higher cooling rates undergone by the material. The micrographs and cooling rates of the samples are in agreement with the average hardness. Hence, using process parameters with reduced heat input, like low wire feed rate or high travel speed, increases the overall microhardness of WAAM deposited samples. The influence of heat input on the average hardness is presented in Fig. 16(c).

Tensile properties

The stress–strain curves measured during tensile testing were analysed to estimate the ultimate tensile strength and elongation after fracture. A comparison of the tensile strengths of samples deposited with varying travel speeds and wire feed rates is shown in Fig. 17. The nominal tensile strength of the ER110S-G wire feed material is 823 MPa. For both horizontally and vertically oriented samples deposited with varying process parameters (wire feed rate and travel speed), it can be observed that samples with heat input less than about 544 J/mm have a tensile strength greater than 823 MPa. Additionally, the tensile strength increases with increased travel speed and a decreased wire feed rate (reduced heat input). Sample S5 (highest travel speed) and S6 (lowest wire feed rate) have tensile strengths of 923 MPa and 897 MPa, respectively. Similar to hardness data, samples S5 and S6 have higher strength because of the higher martensite and bainite phase fractions and refined grain size observed in these samples. This is evident from the micrographs indicated in Fig. 12. Fig. 17(c) indicates the variation

of tensile strength with heat input. Predominantly, horizontally oriented samples have a higher tensile strength than vertically oriented samples. The quadratic trend lines indicate that the increasing heat input above 544 J/mm leads to tensile strength approaching a constant value. It can be observed that the variation of tensile strength is higher in the case of horizontal samples because the horizontal specimens were extracted from different heights along the build direction. Based on Fig. 9 it can be inferred that cooling rates decrease along the build direction. This gradient in cooling rates can give rise to variations in the microstructure across different heights, contributing to the observed differences in tensile strength among horizontal specimens.

For high-strength steels, it is important to determine the elongation to fracture during tensile testing to analyse the ductility and fracture toughness of the material. The elongation to fracture of samples deposited with varying wire feed rates and travel speeds are given in Fig. 18. The samples display good elongation to fracture with values varying from $15.5 \pm 1.8\%$ to $24.9 \pm 0.8\%$. The nominal elongation to fracture of the filler material is 18%. All horizontally oriented samples have higher elongation than 18%. The effect of heat input on the elongation of horizontally and vertically oriented samples is shown in Fig. 18(c). Vertically oriented samples display uniform elongation along with increasing heat input. However, horizontally oriented samples indicate a gradual increase with increasing heat input.

Interestingly, samples S4, S5, S8 and S9 have the highest elongation to fracture (greater than 22%) for horizontal samples. Correlating the elongation values to cooling rates, it can be observed that the highest elongation is observed for the samples which had a cooling rate of less than $10 \text{ }^\circ\text{C/s}$. The microstructural analysis and CCT diagram from Section “Microstructure characterization” indicates the presence of higher fractions of polygonal ferrite, which is soft and possesses high ductility. In addition, samples oriented horizontally tend to have a more uniform microstructure which aids with enhanced plastic deformation during

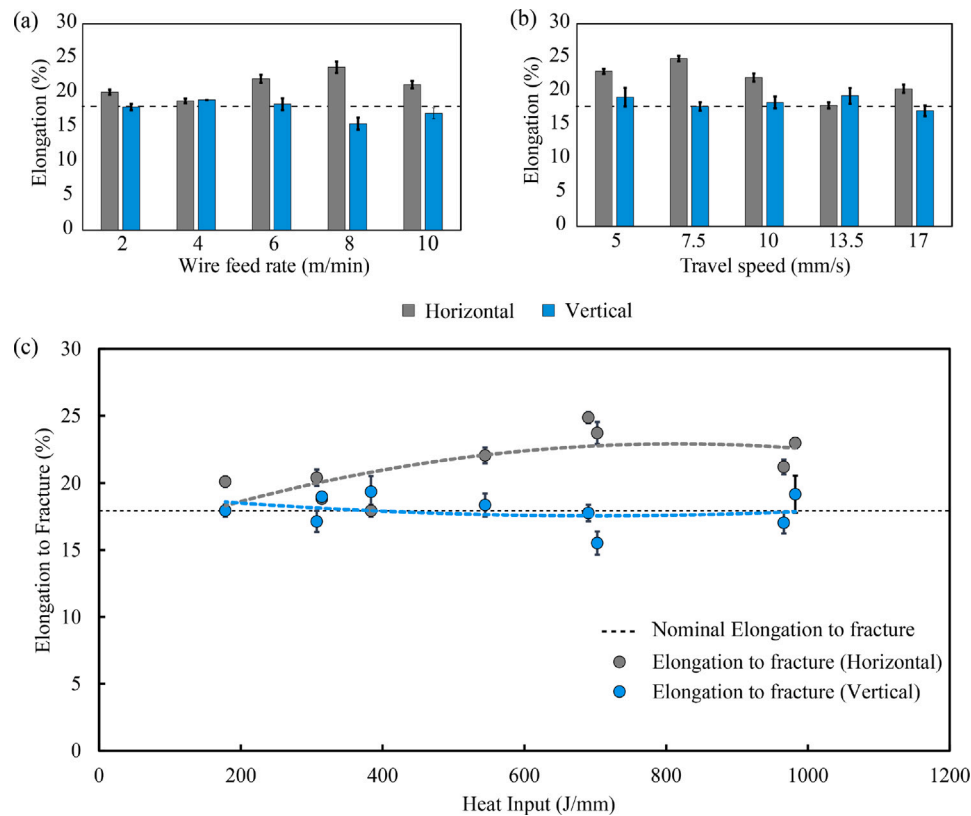


Fig. 18. Elongation of horizontally and vertically oriented samples obtained from stress-strain curves of samples deposited with (a) varying wire feed rate and (b) varying travel speed.

tensile loading. It can also be observed that in all cases, horizontal samples have a higher elongation to fracture than vertical samples. This can be attributed to the higher density of vertically stacked interlayer regions or heat-affected zones within vertical samples. It has been previously identified that interlayer regions (Sun et al., 2020a) or inter-critical/sub-critical heat-affected zones (Lyu et al., 2021; Babu et al., 2023) are associated with localized stress concentrations caused by the presence of lower-strength microstructural constituents along with localized brittle zones such as martensite–austenite islands. Since horizontally oriented samples have a lower density of interlayer regions or heat-affected zones and the loading direction during the tensile test is parallel to the interlayer region they have only a minor effect on anisotropy associated with elongation (Sun et al., 2020a). The effect of vertically stacked interlayers or heat-affected zones is exaggerated in case of high heat input due to lower cooling rates promoting the formation of localized brittle zones and grain coarsening.

Fractography

The presence of a cup and cone fracture surface and a fibrous network of dimples indicate the ductile fracture for all the horizontally aligned samples deposited with different heat inputs as shown in Fig. 19. Microstructural features including grain size and phase fraction influence the appearance of a fracture surface and the geometry of micro-voids or dimples. The staggered fracture surface along with shallow and wider dimples are indicative of a lower ductility for sample S6. Conversely, samples S3 and S1 have a fracture surface characterized by a cup and cone structure. Deeper dimples observed in high heat input samples indicate the higher ductility in samples S3 and S1 due to the higher presence of softer microstructural phases like polygonal ferrite. This is in agreement with the elongation to fracture values observed in Fig. 18

Conclusion

In this study, we investigated the influence of process parameters including wire feed rate and travel speed on the geometry, microstructure and mechanical properties of WAAM-deposited ER110S-G steel. Thin wall structures were deposited with different wire feed rates and travel speeds accompanied by real-time thermal measurements. The geometry of the thin wall structures was analysed and linked to the process parameters. Thermal profiles were correlated to microstructure and mechanical properties. The major conclusions from this work are

- Increasing wire feed rates and reducing travel speeds during the deposition of thin wall structures can enhance their height and effective width. However, when aiming for a high deposition rate, employing a high heat input by increasing the wire feed rate can lead to excessive surface waviness. Conversely, it is more favourable to fabricate samples with lower heat input by reducing the wire feed rates to achieve dimensional accuracy.
- The initial layers of thin walls experience higher cooling rates because the heat diffuses more rapidly towards the substrate. As the layer height increases, the cooling rates gradually decrease and eventually reach a constant value. Independently varying wire feed rate and travel speed affect cooling rates similarly. Nevertheless, adopting higher wire feed rates and lower travel speeds generally results in lower cooling rates.
- Microstructural analysis indicates a mixed microstructure of polygonal ferrite, acicular ferrite, bainite and low-carbon martensite. However, a qualitative microstructural evaluation suggests an increase in acicular ferrite and martensite phase fractions and a reduction in grain size as the heat input decreases. Less than 3% volume fraction of retained austenite is detected in samples deposited with the varying heat inputs evaluated in this study.

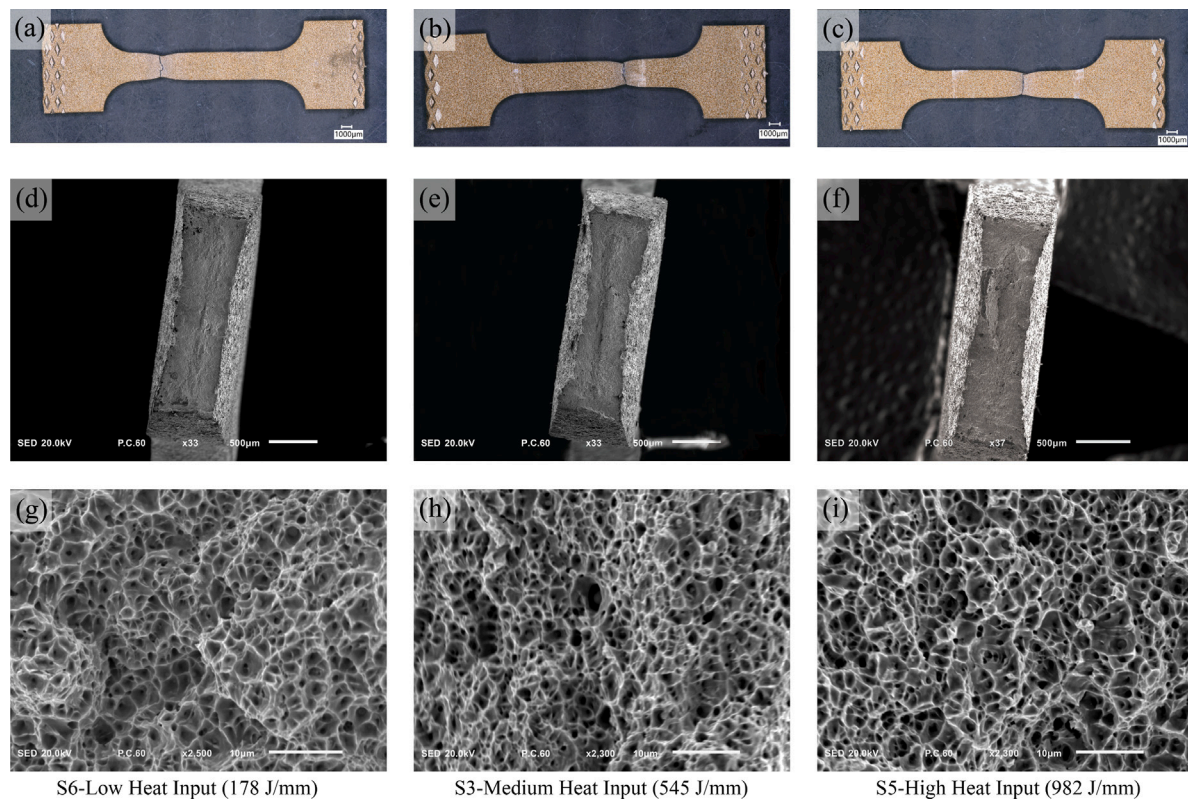


Fig. 19. Fracture surfaces corresponding to tensile test samples oriented along deposition (horizontal) direction fabricated with different heat inputs. (a), (b), (c) indicate the fracture location in horizontal samples corresponding to low, medium and high heat inputs respectively, (d), (e), (f) represent the corresponding fracture surface and (g), (h), (i) are magnified images of fracture surfaces.

- Hardness and tensile strength increase with lower heat input due to higher cooling rates. Samples oriented along the deposition direction have higher strength and elongation due to the orientation of the interlayer regions and inter-critical heat-affected zones perpendicular to build directions. A maximum increase of 12% was observed for low heat input samples oriented along the deposition direction for the tensile strength as the heat input was reduced.

CRediT authorship contribution statement

Aravind Babu: Writing – review & editing, Writing – original draft, Visualization, Validation, Methodology, Investigation, Formal analysis, Data curation, Conceptualization. **Emiliano Trodini:** Methodology, Investigation. **José Luis Galán Argumedo:** Methodology, Investigation, Formal analysis. **Ian M. Richardson:** Writing – review & editing, Supervision, Funding acquisition. **Marcel J.M. Hermans:** Writing – review & editing, Supervision, Software, Resources, Project administration, Methodology, Funding acquisition.

Declaration of competing interest

The authors declare that they have no known competing financial interests or personal relationships that could have appeared to influence the work reported in this paper.

Acknowledgements

This research was carried out under project number P16-46 pr3/S17024j, which is part of the AiM2XL program framework of the Partnership Program of the Materials innovation institute M2i (www.m2i.nl) and the Netherlands Organization for Scientific Research (www.nwo.nl).

The authors extend their gratitude to Mr Ruud Hendriks, from the Department of Materials Science and Engineering at the Delft University of Technology, for his invaluable contribution to the X-ray analysis. They also express their appreciation to Mr Remko Seijffers, also from the same department, for his supportive role during the wire-arc additive manufacturing (WAAM) experiments.

Data availability

Data will be made available on request.

References

- Ahsan, M.R., Fan, X., Seo, G.-J., Ji, C., Noakes, M., Nycz, A., Liaw, P.K., Kim, D.B., 2021. Microstructures and mechanical behavior of the bimetallic additively-manufactured structure (BAMS) of austenitic stainless steel and Inconel 625. *J. Mater. Sci. Technol.* 74, 176–188. <http://dx.doi.org/10.1016/j.jmst.2020.10.001>.
- Ahsan, M.R., Tanvir, A.N., Seo, G.J., Bates, B., Hawkins, W., Lee, C., Liaw, P.K., Noakes, M., Nycz, A., Kim, D.B., 2020. Heat-treatment effects on a bimetallic additively-manufactured structure (BAMS) of the low-carbon steel and austenitic-stainless steel. *Addit. Manuf.* 32, <http://dx.doi.org/10.1016/j.addma.2020.101036>.
- Aldalur, E., Veiga, F., Suárez, A., Bilbao, J., Lamikiz, A., 2020. High deposition wire arc additive manufacturing of mild steel: Strategies and heat input effect on microstructure and mechanical properties. *J. Manuf. Process.* 58, 615–626. <http://dx.doi.org/10.1016/j.jmapro.2020.08.060>.
- Babu, A., Ebrahimi, A., Wu, K.-H., Richardson, I.M., Hermans, M.J., 2023. Local control of microstructure and mechanical properties of high-strength steel in electric arc-based additive manufacturing. *J. Mater. Res. Technol.* 26, 1508–1526. <http://dx.doi.org/10.1016/j.jmrt.2023.07.262>.
- Behrooz, E., 2020. Characterising heat losses in wire and arc additive manufacturing of S690QL high strength steel.
- Bhadeshia, H., Honeycombe, R., 2017. *Steels and properties*.
- Bourlet, C., Zimmer-Chevret, S., Pesci, R., Bigot, R., Robineau, A., Scandella, F., 2020. Microstructure and mechanical properties of high strength steel deposits obtained by Wire-Arc Additive Manufacturing. *J. Mater. Process. Technol.* 285, 116759. <http://dx.doi.org/10.1016/j.jmatprotec.2020.116759>.

- Bradstreet, B., 1968. Effect of surface tension and metal flow on weld bead formation. *Weld. J.* 47 (7), 314s–322s.
- Chandrasekaran, S., Hari, S., Amirthalingam, M., 2020. Wire arc additive manufacturing of functionally graded material for marine risers. *Mater. Sci. Eng. A* 792, <http://dx.doi.org/10.1016/j.msea.2020.139530>.
- Chen, M.-T., Zhang, T., Gong, Z., Zuo, W., Wang, Z., Zong, L., Zhao, O., Hu, L., 2024. Mechanical properties and microstructure characteristics of wire arc additively manufactured high-strength steels. *Eng. Struct.* 300, 117092. <http://dx.doi.org/10.1016/j.engstruct.2023.117092>.
- Dehaghani, M.R., Tang, Y., Panicker, S., Wu, D., Coatanea, E., Wang, G.G., 2023. Modeling and optimization of height-related geometrical parameters for thin wall structures manufactured by metal additive manufacturing. *Int. J. Adv. Manuf. Technol.* 1–13. <http://dx.doi.org/10.1007/s00170-023-12618-0>.
- Dirisu, P., Ganguly, S., Mehmanparast, A., Martina, F., Williams, S., 2019. Analysis of fracture toughness properties of wire+ arc additive manufactured high strength low alloy structural steel components. *Mater. Sci. Eng.: A* 765, 138285. <http://dx.doi.org/10.1016/j.msea.2019.138285>.
- Donoghue, J., Antonysamy, A.A., Martina, F., Colegrove, P.A., Williams, S.W., Prangnell, P., 2016. The effectiveness of combining rolling deformation with Wire–Arc Additive Manufacture on β -grain refinement and texture modification in Ti–6Al–4V. *Mater. Charact.* 114, 103–114. <http://dx.doi.org/10.1016/j.matchar.2016.02.001>.
- Duarte, V.R., Rodrigues, T.A., Schell, N., Santos, T.G., Oliveira, J.P., Miranda, R.M., 2021. Wire and arc additive manufacturing of high-strength low-alloy steel: microstructure and mechanical properties. *Adv. Eng. Mater.* 23 (11), 2001036. <http://dx.doi.org/10.1002/adem.202001036>.
- Ermakova, A., Mehmanparast, A., Ganguly, S., Razavi, J., Berto, F., 2020. Investigation of mechanical and fracture properties of wire and arc additively manufactured low carbon steel components. *Theor. Appl. Fract. Mech.* 109, 102685. <http://dx.doi.org/10.1016/j.tafmec.2020.102685>.
- Fang, Q., Zhao, L., Chen, C.-x., Cao, Y., Song, L., Peng, Y., Yin, F.-x., 2022. 800 MPa class HSLA steel block part fabricated by WAAM for building applications: Tensile properties at ambient and elevated (600°C) temperature. *Adv. Mater. Sci. Eng.* 2022, <http://dx.doi.org/10.1155/2022/3014060>.
- Fang, Q., Zhao, L., Chen, C., Zhu, Y., Peng, Y., Yin, F., 2023. Effect of heat input on microstructural and mechanical properties of high strength low alloy steel block parts fabricated by wire arc additive manufacturing. *Mater. Today Commun.* 34, 105146. <http://dx.doi.org/10.1016/j.mtcomm.2022.105146>.
- Fu, J., Brouwer, J., Richardson, I., Hermans, M., 2019. Effect of mechanical alloying and spark plasma sintering on the microstructure and mechanical properties of ODS Eurofer. *Mater. Des.* 177, 107849. <http://dx.doi.org/10.1016/j.matdes.2019.107849>.
- Geng, H., Li, J., Xiong, J., Lin, X., Huang, D., Zhang, F., 2018. Formation and improvement of surface waviness for additive manufacturing 5A06 aluminium alloy component with GTAW system. *Rapid Prototyp. J.* <http://dx.doi.org/10.1108/RPJ-04-2016-0064>.
- Ghaffari, M., Vahedi Nemani, A., Rafieezad, M., Nasiri, A., 2019. Effect of solidification defects and HAZ softening on the anisotropic mechanical properties of a wire arc additive-manufactured low-carbon low-alloy steel part. *Jom* 71, 4215–4224. <http://dx.doi.org/10.1007/s11837-019-03773-5>.
- Gisario, A., Kazarian, M., Martina, F., Mehrpouya, M., 2019. Metal additive manufacturing in the commercial aviation industry: A review. *J. Manuf. Syst.* 53, 124–149. <http://dx.doi.org/10.1016/j.jmsy.2019.08.005>.
- Haden, C., Zeng, G., Carter III, F., Ruhl, C., Krick, B., Harlow, D., 2017. Wire and arc additive manufactured steel: Tensile and wear properties. *Addit. Manuf.* 16, 115–123. <http://dx.doi.org/10.1016/j.addma.2017.05.010>.
- Henckell, P., Gierth, M., Ali, Y., Reimann, J., Bergmann, J.P., 2020. Reduction of energy input in wire arc additive manufacturing (WAAM) with gas metal arc welding (GMAW). *Materials* 13 (11), 2491. <http://dx.doi.org/10.3390/ma13112491>.
- Huang, C., Kyvelou, P., Gardner, L., 2023. Stress-strain curves for wire arc additively manufactured steels. *Eng. Struct.* 279, 115628. <http://dx.doi.org/10.1016/j.engstruct.2023.115628>.
- Kumar, A., DebRoy, T., 2006. Toward a unified model to prevent humping defects in gas tungsten arc welding. *Welding J.* 85 (12), 292.
- Lyu, Z., Sato, Y.S., Tokita, S., Zhao, Y., Jia, J., Wu, A., 2021. Microstructural evolution in a thin wall of 2Cr13 martensitic stainless steel during wire arc additive manufacturing. *Mater. Charact.* 182, 111520. <http://dx.doi.org/10.1016/j.matchar.2021.111520>.
- Mishra, V., Babu, A., Schreurs, R., Wu, K., Hermans, M., Ayas, C., 2023. Microstructure estimation and validation of ER110s-G steel structures produced by wire and arc additive manufacturing. *J. Mater. Res. Technol.* 23, 3579–3601. <http://dx.doi.org/10.1016/j.jmrt.2023.01.214>.
- Müller, J., Grabowski, M., Müller, C., Hensel, J., Unglaub, J., Thiele, K., Kloft, H., Dilger, K., 2019. Design and parameter identification of wire and arc additively manufactured (WAAM) steel bars for use in construction. *Metals* 9 (7), 725. <http://dx.doi.org/10.3390/met9070725>.
- Nemani, A.V., Ghaffari, M., Nasiri, A., 2020. Comparison of microstructural characteristics and mechanical properties of shipbuilding steel plates fabricated by conventional rolling versus wire arc additive manufacturing. *Addit. Manuf.* 32, 101086. <http://dx.doi.org/10.1016/j.addma.2020.101086>.
- Norrish, J., 2017. Recent gas metal arc welding (GMAW) process developments: the implications related to international fabrication standards. *Weld. the World* 61, 755–767. <http://dx.doi.org/10.1007/s40194-017-0463-8>.
- Norrish, J., Polden, J., Richardson, I., 2021. A review of wire arc additive manufacturing: development, principles, process physics, implementation and current status. *J. Phys. D: Appl. Phys.* 54 (47), 473001. <http://dx.doi.org/10.1088/1361-6463/ac1e4a>.
- Pal, K., Pal, S.K., 2011. Effect of pulse parameters on weld quality in pulsed gas metal arc welding: A review. *J. Mater. Eng. Perform.* 20 (6), 918–931. <http://dx.doi.org/10.1007/s11665-010-9717-y>.
- Panchenko, O., Kládov, I., Kurushkin, D., Zhabrev, L., Ryl'kov, E., Zamozdra, M., 2022. Effect of thermal history on microstructure evolution and mechanical properties in wire arc additive manufacturing of HSLA steel functionally graded components. *Mater. Sci. Eng.: A* 851, 143569. <http://dx.doi.org/10.1016/j.msea.2022.143569>.
- Rafieezad, M., Ghaffari, M., Vahedi Nemani, A., Nasiri, A., 2019. Microstructural evolution and mechanical properties of a low-carbon low-alloy steel produced by wire arc additive manufacturing. *Int. J. Adv. Manuf. Technol.* 105, 2121–2134. <http://dx.doi.org/10.1007/s00170-019-04393-8>.
- Rodrigues, T.A., Duarte, V., Avila, J.A., Santos, T.G., Miranda, R., Oliveira, J., 2019. Wire and arc additive manufacturing of HSLA steel: Effect of thermal cycles on microstructure and mechanical properties. *Addit. Manuf.* 27, 440–450. <http://dx.doi.org/10.1016/j.addma.2019.03.029>.
- Rodrigues, T.A., Duarte, V., Tomás, D., Avila, J.A., Escobar, J., Rossinyol, E., Schell, N., Santos, T.G., Oliveira, J., 2020. In-situ strengthening of a high strength low alloy steel during Wire and Arc Additive Manufacturing (WAAM). *Addit. Manuf.* 34, 101200. <http://dx.doi.org/10.1016/j.addma.2020.101200>.
- Sampaio, R., Pragana, J., Bragança, I., Silva, C., Nielsen, C., Martins, P., 2023. Modelling of wire-arc additive manufacturing – A review. *Adv. Ind. Manuf. Eng.* 6, 100121. <http://dx.doi.org/10.1016/j.aime.2023.100121>.
- Scotti, F.M., Teixeira, F.R., da Silva, L.J., de Araujo, D.B., Reis, R.P., Scotti, A., 2020. Thermal management in WAAM through the CMT advanced process and an active cooling technique. *J. Manuf. Process.* 57, 23–35. <http://dx.doi.org/10.1016/j.jmapro.2020.06.007>.
- da Silva, L.J., Souza, D.M., de Araújo, D.B., Reis, R.P., Scotti, A., 2020. Concept and validation of an active cooling technique to mitigate heat accumulation in WAAM. *Int. J. Adv. Manuf. Technol.* 107 (5–6), 2513–2523. <http://dx.doi.org/10.1007/s00170-020-05201-4>.
- Sun, L., Jiang, F., Huang, R., Yuan, D., Guo, C., Wang, J., 2020a. Anisotropic mechanical properties and deformation behavior of low-carbon high-strength steel component fabricated by wire and arc additive manufacturing.
- Sun, L., Jiang, F., Huang, R., Yuan, D., Guo, C., Wang, J., 2020b. Microstructure and mechanical properties of low-carbon high-strength steel fabricated by wire and arc additive manufacturing. *Metals* 10 (2), 216. <http://dx.doi.org/10.3390/met10020216>.
- Sun, L., Jiang, F., Huang, R., Yuan, D., Su, Y., Guo, C., Wang, J., 2020c. Investigation on the process window with liner energy density for single-layer parts fabricated by wire and arc additive manufacturing. *J. Manuf. Process.* 56, 898–907. <http://dx.doi.org/10.1016/j.jmapro.2020.05.054>.
- Thompson, S.W., Colvin, D.J., Krauss, G., 1996. Austenite decomposition during continuous cooling of an HSLA-80 plate steel. *Met. Mater. Trans. A* 27 (6), 1557–1571. <http://dx.doi.org/10.1007/BF02649815>.
- Thompson, S.W., Vin Col, D.J., Krauss, G., 1990. Continuous cooling transformations and microstructures in a low-carbon, high-strength low-alloy plate steel. *Met. Trans. A* 21 (6), 1493–1507. <http://dx.doi.org/10.1007/BF02672564>.
- Vahedi Nemani, A., Ghaffari, M., Salahi, S., Lunde, J., Nasiri, A., 2021. Effect of interpass temperature on the formation of retained austenite in a wire arc additive manufactured ER420 martensitic stainless steel. *Mater. Chem. Phys.* 266, 124555. <http://dx.doi.org/10.1016/j.matchemphys.2021.124555>.
- Wu, B., Pan, Z., Ding, D., Cuiuri, D., Li, H., Xu, J., Norrish, J., 2018. A review of the wire arc additive manufacturing of metals: properties, defects and quality improvement. *J. Manuf. Process.* 35, 127–139. <http://dx.doi.org/10.1016/j.jmapro.2018.08.001>.
- Wu, B., Qiu, Z., Pan, Z., Carpenter, K., Wang, T., Ding, D., Duin, S.V., Li, H., 2020. Enhanced interface strength in steel-nickel bimetallic component fabricated using wire arc additive manufacturing with interweaving deposition strategy. *J. Mater. Sci. Technol.* 52, <http://dx.doi.org/10.1016/j.jmst.2020.04.019>.
- Xu, X., Ding, J., Ganguly, S., Diao, C., Williams, S., 2019. Preliminary investigation of building strategies of maraging steel bulk material using wire + arc additive manufacture. *J. Mater. Eng. Perform.* 28 (2), <http://dx.doi.org/10.1007/s11665-018-3521-5>.
- Yildiz, A.S., Davut, K., Koc, B.ş., Yilmaz, O., 2020. Wire arc additive manufacturing of high-strength low alloy steels: study of process parameters and their influence on the bead geometry and mechanical characteristics. *Int. J. Adv. Manuf. Technol.* 108 (11–12), 3391–3404. <http://dx.doi.org/10.1007/s00170-020-05482-9>.
- Zhai, W., Wu, N., Zhou, W., 2022. Effect of interpass temperature on wire arc additive manufacturing using high-strength metal-cored wire. *Metals* 12 (2), 212. <http://dx.doi.org/10.3390/met12020212>.